

Corrosion Behavior of Austenitic Stainless Steel Welds Prepared by Dual Protection GTAW Process in 0.5 M H₂SO₄ and 3.5%wt. NaCl

Laura Lima, Leonel Dimas Abreu, Cristiana Brasil Maia, Pedro Brito*

Pontifical Catholic University of Minas Gerais, Department of Mechanical Engineering, Av. Dom José Gaspar 500, CEP 30535-901, Belo Horizonte (MG), Brazil.

*E-mail: ppbrito@gmail.com

Received: 5 January 2019 / *Accepted:* 17 March 2019 / *Published:* 7 October 2019

The GTAW process is largely employed in the industry for welding metal alloys and is generally considered to generate high quality welds with relatively low penetration in comparison to other arc-welding processes. In the present study, a modified GTAW dual shielding torch operating with an inner flow of pure Ar gas and an outer flow of mixed Ar-CO₂ gas was employed for producing autogenous AISI 316L stainless steel bead-on-plate welds. The performance of the proposed torch was assessed by numerical simulation of the gas flow in the nozzle, microstructure characterization and corrosion resistance analysis. To this end, a number of welds were produced with different levels of CO₂ concentration in the outer gas layer (0, 1, 2.5, 4, 8, 15, 25, 50 and 100%) and the samples were analyzed in terms of optical microscopy and X-ray Diffraction. When using the modified nozzle with a 2.5% CO₂ concentration in the outer gas flow, an increase of 2.5 times in the weld depth/width ratio could be obtained in relation to the pure Ar shielding condition. With the proposed configuration, no significant changes in phase composition or microstructure were noticed relative to the standard 100% Ar welding condition, and the samples were also found to exhibit similar corrosion behavior.

Keywords: GTAW, dual shielding, active gas, stainless steel, weld penetration.

1. INTRODUCTION

The Gas Tungsten Arc Welding (GTAW) process is currently one of the most applied welding techniques for joining stainless steels because of weld metal and surface quality [1]. The heat necessary for the weld is obtained by an electric arc established between the workpiece and a non-consumable tungsten electrode. In order to avoid electrode degradation, inert shielding gases such as argon or helium are used, as well as low welding current values. This leads to lower weld penetration and metal deposition rates compared to *e.g.* Gas Metal Arc Welding (GMAW) or Plasma Arc Welding (PAW) [2].

According to Heiple and Roper [3,4], GTAW productivity may be enhanced by the addition of surface active elements such as oxygen or sulfur to the weld pool, which alter molten metal convection, increasing heat transfer to the inferior portions of the welded joint and improving penetration [5,6]. This was first accomplished by employing active fluxes (Active-GTAW or A-GTAW), which can significantly increase penetration thanks to a combination of electric arc constriction and Marangoni convection effects [7–10]. It has been observed, however, that the efficiency of the A-GTAW process is sensitive to flux particle size and quantity, which can be difficult to control in industrial practice [9,11].

A recent alternative to promote the incorporation of surface active elements in the weld pool is the addition of active gases in the inert gas shielding (activating arc) [12–14]. Preparation and application of the active/inert gas mixture can be controlled more efficiently in comparison to the solid flux and can also be automatized. The utilization of active gases, even in small amounts, however, leads to severe oxidation of the tungsten electrode. Recently, in order to avoid electrode degradation, a modified GTAW torch was proposed to produce dual shielding gas that consisted of an internal pure inert gas layer for electrode protection and an external active/inert gas mixture through which active elements are injected into the weld pool [2,11,15,16].

The dual shielding GTAW process has so far been applied to welding austenitic [11,15,17] and duplex stainless steels [16,18] and it has been possible to confirm the expected increase in weld penetration. However, the influence of this process on the actual corrosion resistance of the stainless steel welded joints remains yet to be explored. This is an important aspect to be considered since previous investigations on the A-GTAW process have shown that increasing oxygen content in the weld is detrimental to corrosion resistance [8]. Based on this premise, in the present work a modified GTAW torch is proposed and analyzed for welding AISI 316L austenitic stainless steels with varying levels of CO₂ gas. The effects of dual shielding on weld geometry, microstructure and corrosion behavior were analyzed and it is expected that the results obtained might assist further developments using active gases in the GTAW process.

2. EXPERIMENTAL PROCEDURE

2.1. Materials

The materials used in the welding experiments were 150 x 20 x 11 mm AISI 316L stainless steel plates with chemical composition presented in Table 1. Prior to welding, the plates were annealed at 1100°C for 30 minutes, quenched in water for microstructure homogenization and the metal surfaces were machined and cleaned in acetone. For the GTAW process, W-2%ThO₂ electrodes with 2.4 mm diameter and 60° tip angle were used. The electrodes were weighted before and after each welding operation.

Table 1. Chemical composition of the AISI 316L steel used in the welding experiments (wt.%)

C	Mn	Si	P	S	Cr	Ni	Mo	Cu	N	Fe
0.008	1.21	0.302	0.023	0.001	16.84	10.10	1.99	0.1745	0.030	Bal.

A model of the proposed geometry for the dual shielding torch is presented in Figure 1 (the solid portions in represent the regions in which gas flow takes place) and the dimensions of the nozzle are presented in Figure 2. The external Ar-CO₂ gas is fed laterally from below the pure Ar injection point, as illustrated in Figure 1, via four circular inlets positioned symmetrically around the torch.

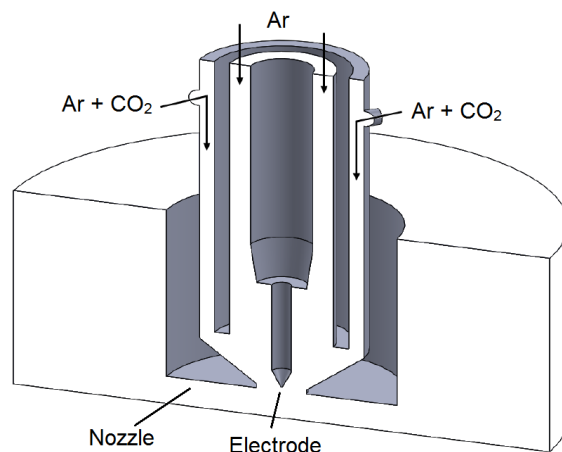


Figure 1. Model for the dual shielding torch

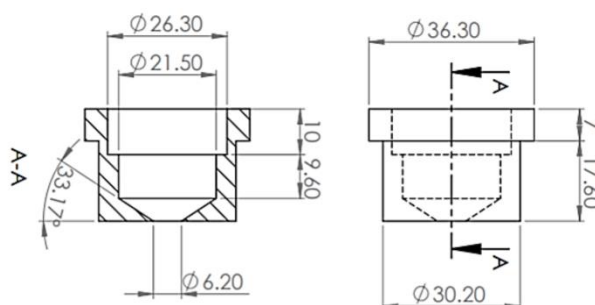


Figure 2. Nozzle design with dimensions

2.2. Welding parameters

The welding procedures were performed on an automatized welding station, with an 10 l/min gas flow (for both active and inert gases), welding speed of 2 mm/s and welding current of 80 A. The electrode/workpiece distance was set at 4 mm. Bead-on-plate welds were performed for each case with a total length of 100 mm (welding time of 50 s per weld). The remaining parameters (active gas composition, arc voltage and heat input) are summarized in Table 2.

2.3. Microstructure characterization

Cross-section samples were taken from selected welds and from the AISI 316L base material and analyzed by optical microscopy. The preparation procedure involved grinding and polishing to a 3 μm finish in diamond suspension and etching in Kalling's reagent (100 ml ethylic alcohol, 100 ml HCl and

5 g CuCl₂) by immersion for 5 minutes. Quantitative phase analysis was performed by X-ray Diffraction (XRD) and the results were compared with those obtained with a ferriscope (10 measurements per sample). The XRD analyses were performed using a Cu K_α source, operating at 40.0 kV and 30 mA, with a diffraction angle (2θ) measurement range of 35 to 90°, 0.02° step and 2°/s measurement speed.

Table 2. Summary of welding parameters (E – arc voltage, HI – heat input)

Active gas	E (V)	HI (J/mm)
Ar-0% CO ₂	14.7	588
Ar-1% CO ₂	14.7	588
Ar-2.5% CO ₂	15.5	620
Ar-4% CO ₂	16.0	640
Ar-8% CO ₂	16.5	660
Ar-15% CO ₂	16.2	648
Ar-25% CO ₂	17.2	688
Ar-50% CO ₂	16.5	660
Ar-100% CO ₂	17.0	680

2.4. Electrochemical corrosion behavior

In order to evaluate whether dual shielding with active gas could be detrimental to corrosion resistance, the electrochemical behavior of the base material and welded samples obtained with 2.5% CO₂+Ar and 100% Ar gas was compared. The experiments were performed in an IVIUM Vertex potentiostat/galvanostat connected to a horizontal cell for flat specimens with 400 ml capacity at room temperature (25±1°C). A three electrode setup was employed with a square 10x10 mm Pt foil as counter electrode and Ag-AgCl in saturated KCl reference electrode. Investigations were performed in H₂SO₄ 0.5 M and 3.5% wt. NaCl (both containing naturally dissolved O₂) before which the sample surface was prepared by grinding and polishing. The open circuit potential (OCP) was monitored for 1.5 h and then potentiodynamic polarization scans were performed with 0.2 mV/s scan rate for determining corrosion current density (*i*_{corr}), corrosion potential (*E*_{corr}) and pitting potential (*E*_{pit}).

3. NUMERICAL ANALYSIS

Numerical analysis of the gas flow was performed using Ansys Fluent®. A tetrahedral mesh was used, which was refined at regions of interest (notably at the gas exit point). Overall, a total of 454,709 elements and 167,384 nodes were used. The mathematic model is described by the Navier-Stokes and continuity equations, for a compressible flow operating in steady-state conditions. In order to take into account the turbulence effects, the k-ε model was used. Atmospheric pressure was set at 0 Pa, gravity acceleration at 9.81 m/s², gas temperature at 300 K and the walls were considered adiabatic and gas flow, at the positions indicated in Figure 1, was set at 10 l/min for both gas mixtures. The simulations were

performed for two inert/active gas compositions: Ar-(Ar+1%CO₂) and Ar-100%CO₂. For both cases, copper was adopted as the nozzle material.

4. RESULTS AND DISCUSSION

4.1. Gas flow simulation

The results of the gas flow simulation are presented in Figure 3(a) and (b) considering the 1%CO₂ and 100%CO₂ active gas compositions, respectively. In the case of Figure 3(a), because of the relatively smaller amount of CO₂, the scale was adjusted between 0 and 0.01 (1%) in order to allow the visualization of the gas composition throughout the nozzle.

The nozzle outlet has a 6.2 mm diameter, which is close to the value of the weld bead width. As such, based on the results presented in Figures 3(a) and (b), it is possible to conclude that, according to the numerical analysis, the gas surrounding the weld pool was enriched with CO₂. For the 1%CO₂ configuration, Figure 3(a), the amount of CO₂ at the nozzle extremities is of the order of 0.1% whereas for the 100%CO₂ configuration the amount of CO₂ present was of the order of 1%. In addition, the results presented in Figure 3(a) and (b) indicate that for both conditions, the tungsten electrode remained isolated from the active gases.

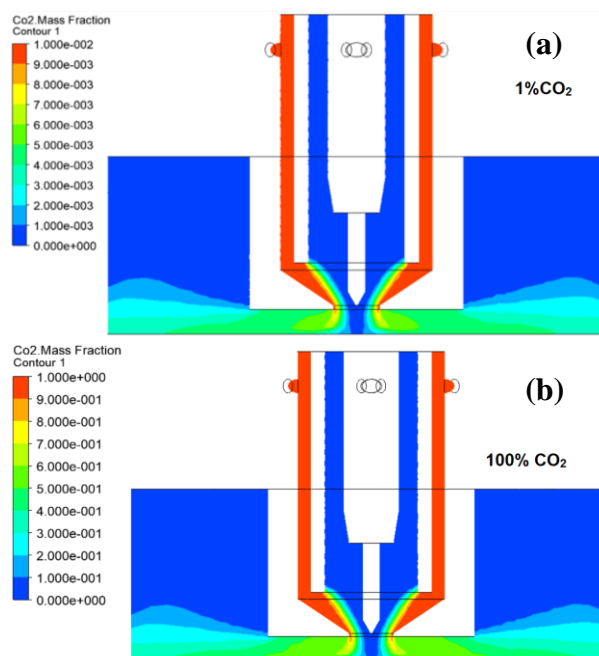


Figure 3. Numerical analysis of dual shielding flow, composition gradients.

In Figure 4(a) and (b), the gas flow behavior is presented in terms of velocity fields for the 1%CO₂ and 100%CO₂ concentrations, respectively. In both cases, the inert gas flow is laminar with maximum velocity at the nozzle exit point, because of the reduced diameters in these sections as observed, for example, by Campbell and co-workers [19]. It is also possible to notice that the active gas

flow is significantly influenced by the inclination of the injection chutes, leading to a spiral flow along the nozzle which was more intense for the 100%CO₂ condition. According to the orientation of the velocity lines at the nozzle exit, it is possible to conclude that the inert and active gas flows become mixed before reaching the fusion zone. The results also show that the gas flow rates inside the nozzle and near the exit point, close to the electrode tip, are not influenced by the active shielding gas composition, with similar values for the velocity fields being obtained for the 1% and 100%CO₂ concentrations. The values calculated for the gas velocity close to the electrode tip agreed with previous simulations of the gas flow performed for the Gas Metal Arc Welding (GMAW) process [20].

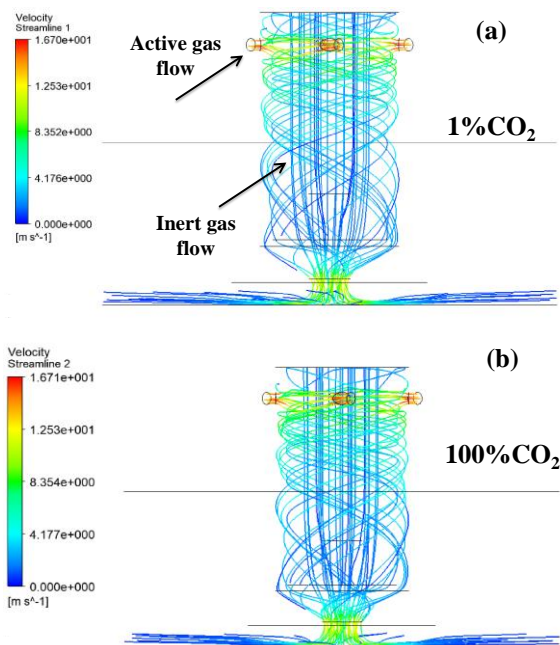


Figure 4. Numerical analysis of dual shielding flow, velocity fields.

4.2. Weld bead geometry

The cross-section macrographs obtained from the nine different tested welding conditions are presented in Figure 5 and the variation of weld width and penetration with CO₂ in the outer gas layer is analyzed in Figure 6(a). From the results presented in Figure 5, it is possible to notice that for 100%Ar and 1%CO₂ concentrations, the weld beads remained shallow and wide. When the CO₂ content was varied between 2.5 and 15%, weld penetration was increased and for 2.5%CO₂ the maximum penetration-to-width ratio was obtained (0.37), which was almost 3 times larger than the ratio obtained for 100%Ar (0.13). This observation converges with the results of the investigations performed by Ahmadi and Ebrahimi [21], who showed that for oxygen concentration levels of up to approximately 150 ppm were correlated with increased penetration-width ratios, but for higher levels penetration was reduced. A possible reason for this behavior is that for relatively low concentrations, oxygen is found to be uniformly distributed throughout the weld pool but for larger values the distribution becomes inhomogeneous which reverses fluid flow in the weld pool [22].

For higher CO₂ concentrations (from 8 to 100%), the penetration-to-width ratio was reduced, but remained consistently above the level registered for 100%Ar shielding. In these cases, it was possible to notice that the overall fusion zone volume increased compared to the 100%Ar configuration. This is probably caused by the increase in arc voltage during welding with a corresponding elevation in heat input (Table 2), given that the welding current remained constant for all cases at 80 A. The reason for this behavior is that the presence of increasing levels of active gas requires higher voltage levels to balance the energy involved in the dissociation of CO₂ molecules [23].

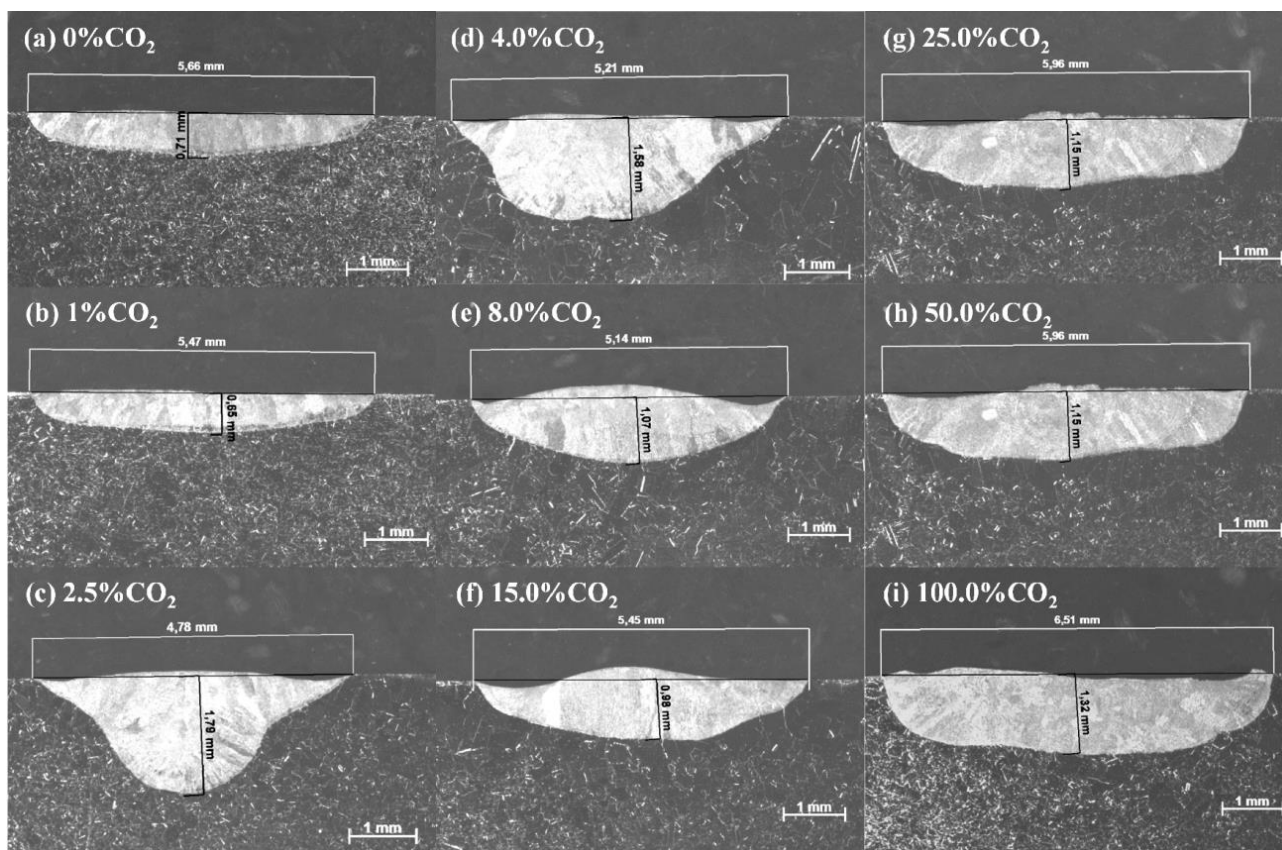


Figure 5. Cross section macrographs of welds obtained using CO₂ levels of: (a) 0%, (b) 1%, (c) 2.5%, (d) 4.0%, (e) 8.0%, (f) 15.0%, (g) 25.0%, (h) 50.0% and (i) 100%.

In a previous investigation [15], a 2.15 increase in penetration-to-width ratio in comparison to conventional GTAW of AISI 304 stainless steels was obtained by applying an external shielding gas layer of 100%CO₂. There is a quantitative difference relative to the present work, in which the maximum gain in penetration was noticed for a relatively lower CO₂ concentration of 2.5% - an indication that the differences in oxygen incorporation in the weld pool are expected to be influenced by nozzle geometry. The increase in penetration is also consistent with observations of the active-GTAW process when employing different oxide fluxes [24].

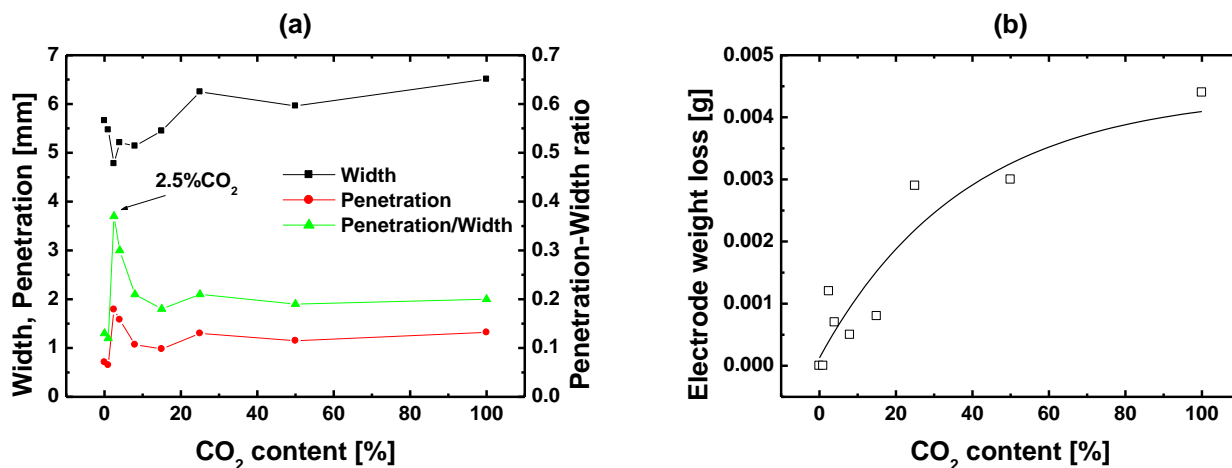


Figure 6. Influence of CO₂ concentration on: (a) weld geometry and (b) electrode oxidation.

The morphology of the tungsten electrodes observed after each welding operation is registered in Figure 7 and in Figure 6(b) the corresponding weight loss as a function of CO₂ content is presented. For concentrations inferior to 15%CO₂, the electrodes remained visually unaltered by the welding process, with an average mass loss lower than 0.0008 g (0.0073% of the total electrode mass). Even though the values are reduced, the results suggest that either nozzle geometry, gas flow rates or even the electrode position could be optimized in order to more effectively protect the tungsten electrode. For example, by increasing the flow rate of the pure Ar shielding gas, contamination by external gases could be avoided and assist the maintenance of a protective atmosphere surrounding the electrode tip [20]. For 0 and 1%CO₂, no observable mass loss due to oxidation could be detected. However, for concentrations over 25%CO₂ the electrodes were clearly deteriorated, indicating that the internal Ar shielding was not capable of completely isolating the active gas, contrary to the results of the numerical analysis.

4.3. Microstructure analysis

Based on the results presented in Figure 5, further analyses were conducted to analyze the microstructure of the welds produced with 2.5%CO₂, which revealed the highest penetration-to-width ratio, in comparison to the sample obtained with pure Ar shielding (0%CO₂). The characteristics of the interface between the Fusion Zone (FZ) and Base Material (BM) are analyzed in Figures 8(a) and (b) for the 0%CO₂ and 2.5%CO₂ welds, respectively. Further examination of the center of the FZ is provided in Figures 8(c) and (d) for the 0%CO₂ and 2.5%CO₂ welds, respectively. Concerning the FZ/BM interface – Figure 8(a) and (b) – it is possible to notice the predominantly single-phase microstructure of the AISI 316L base material (lower portion), with the presence equiaxed austenite grains. At the interface with the FZ, a combination of fine austenite grains and dendrites oriented towards the weld center can be noticed, with signs of epitaxial growth.

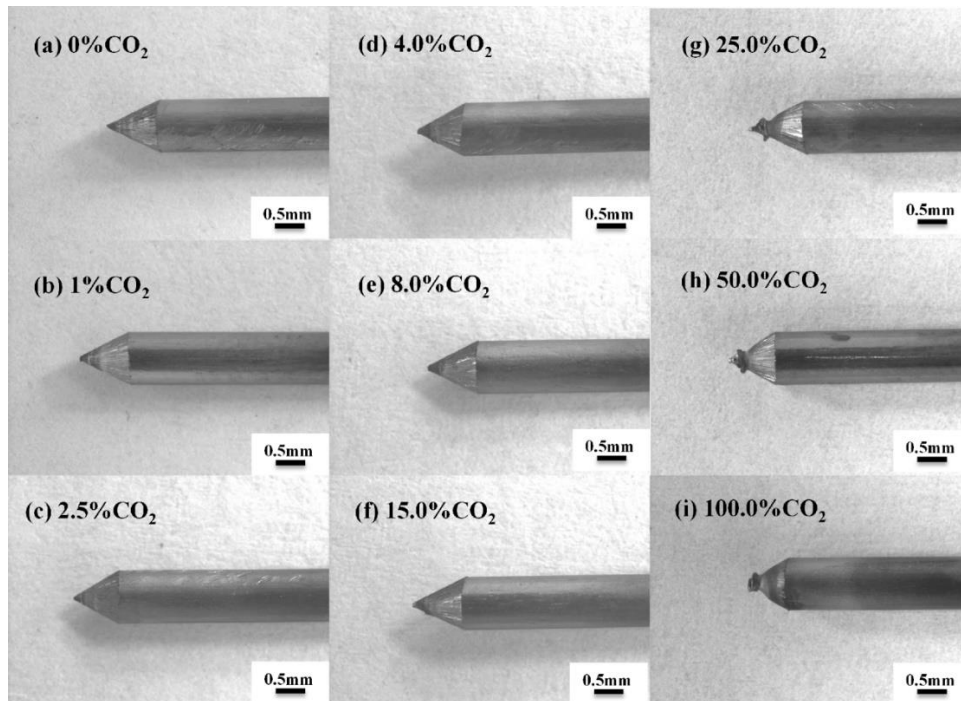


Figure 7. Electrode morphology obtained after welding with CO₂ levels of: (a) 0%, (b) 1%, (c) 2.5%, (d) 4.0%, (e) 8.0%, (f) 15.0%, (g) 25.0%, (h) 50.0% and (i) 100%.

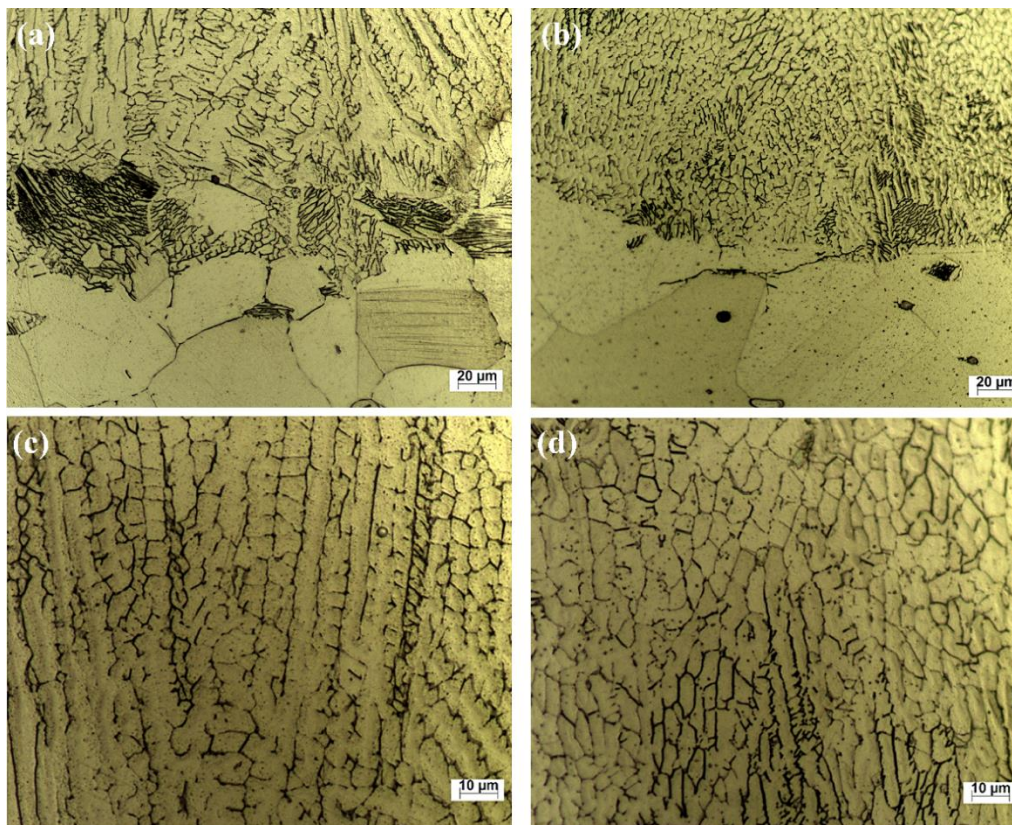


Figure 8. Fusion zone microstructure (cross-sections): (a) BM/FZ interface, 0%CO₂, (b) BM/FZ interface, 2.5%CO₂, (c) FZ 0%CO₂ and (d) FZ 2.5%CO₂.

The microstructure at the center of the FZ is dominated by austenite dendrites with the presence of δ -ferrite along the boundaries (regions with dark contrast) [25]. The AISI 316L steel used in this investigation exhibits Cr_{eq} and Ni_{eq} values of, respectively, 19.28 and 10.94 which corresponds to a ferritic-austenitic primary solidification mode. Thus, phase evolution during solidification can be assumed to follow the order $L \rightarrow L+\delta \rightarrow L+\delta+\gamma \rightarrow \delta+\gamma$ and during cooling $\delta \rightarrow \gamma$ takes place. This mechanism is consistent with the microstructure observed on both analyzed welds (0% and 2.5% CO_2). In order to evaluate quantitative differences in the phase composition of the welds, samples were further examined by XRD and the results are presented in Figure 9. It is possible to notice the presence of δ -ferrite as a minority phase in the welded materials by the presence of the weak (110) reflection, which is absent in the AISI 316L base material. In principle, the results do not show signs of changes in crystallographic orientation, with all reflections following approximately similar proportions with the base material. A summary of the quantitative phase analysis performed by XRD and by employing a ferritoscope is presented in Table 10. It was revealed that both welds exhibited small fractions of δ -ferrite, within the range of 2-6%. In this sense, it is possible to conclude that the 2.5% CO_2 concentration did not lead to significant microstructure alterations in the AISI 316L stainless steel welds, in comparison to the purely 0% CO_2 condition. It is worth noticing that the presence of δ -ferrite (up to 8%) in austenitic stainless steel welds is common and regarded as important to avoid solidification cracking [21].

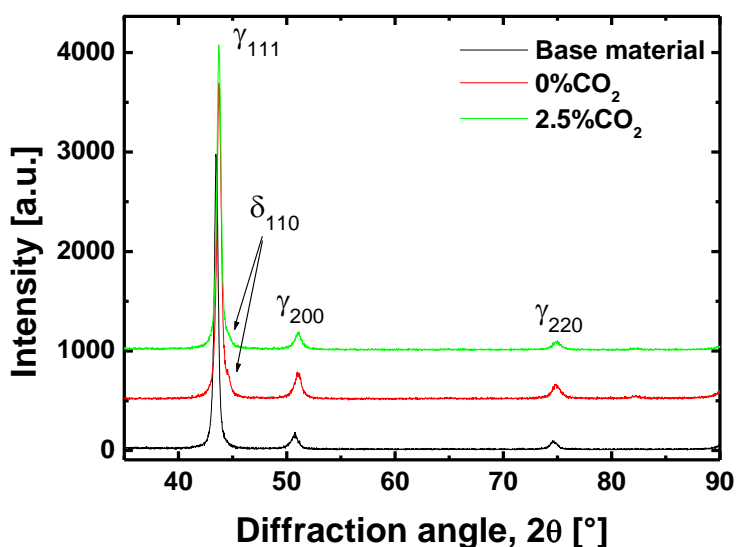


Figure 9. XRD patterns obtained from the 316L base material, 0% CO_2 and 2.5% CO_2 welds.

Table 3. Quantitative phase analysis performed on the 316L base material, 0% CO_2 and 2.5% CO_2 .

Sample	γ/δ balance (XRD)	δ fraction (ferritoscope)
BM	100%/0%	0.204 ± 0.12
1.0% CO_2	95.8%/4.2%	5.93 ± 0.19
2.5% CO_2	97.4%/2.6%	5.85 ± 0.45

4.4. Corrosion behavior

The electrochemical corrosion behavior of the base metal, 0%CO₂ and 2.5%CO₂ welds is analyzed in Figure 10(a-d), which present the evolution of OCP in 0.5M H₂SO₄ and 3.5wt.% NaCl; and the polarization diagrams in 0.5M H₂SO₄ and 3.5wt.% NaCl, respectively. For both electrolytes, in all tested conditions, the OCP values were stabilized after 5,400 s exposure with less than 5 mV/hour variations. The results obtained from the polarization diagrams are summarized in Table 4.

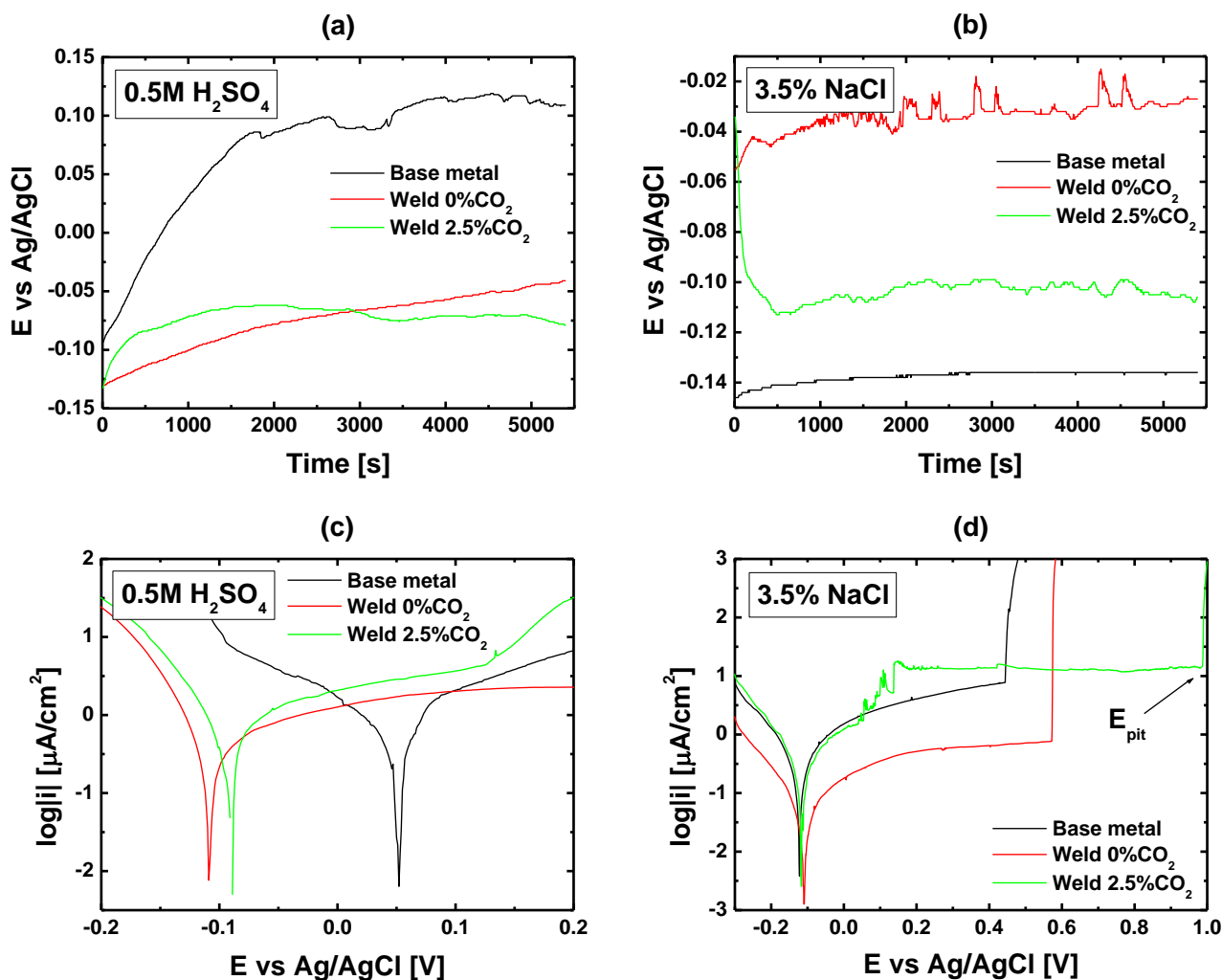


Figure 10. Electrochemical corrosion analysis: (a) OCP evolution in 0.5M H₂SO₄, (b) OCP evolution in 3.5wt.% NaCl, (c) polarization curves in 0.5M H₂SO₄ and (d) polarization curves in 3.5wt.% NaCl.

The results obtained from the polarization tests reveal that all materials exhibited active/passive behavior in both electrolytes. In the case of the 0.5M H₂SO₄ solution, the passive range was extended to close to 1.2V vs. Ag/AgCl, which corresponds to the oxygen reduction reaction (not shown in Figure 10, which highlights instead the Tafel region). The data presented in Figure 10(c) was used for determining the resistance to uniform corrosion in acid media, based on the corrosion current density

(i_{corr}) and corrosion potential (E_{corr}), registered in Table 4. It is possible to notice that the 316L base material exhibited more cathodic behavior in the tested solution, with more positive E_{corr} values, indicating a less reactive metal surface. According to Ramkumar and co-workers [8], this is caused by the higher level of oxygen present in the welds. It is also important to consider the higher amounts of δ -ferrite in the welded zones, which may lead to galvanic interactions with the austenite matrix [26]. The difference is, however, small, and in fact falls in the range of the experimental standard deviation (determined from three measurements), indicating that the welding process did not lead to significant modifications concerning chemical activity.

Table 4. Results of potentiodynamic polarization tests performed on base material and selected welding conditions in 0.5M H₂SO₄ and 3.5wt.% NaCl solutions.

Sample	0.5M H ₂ SO ₄		3.5wt.% NaCl		
	E_{corr} (V)	i_{corr} ($\mu\text{A}/\text{cm}^2$)	E_{corr} (V)	i_{corr} ($\mu\text{A}/\text{cm}^2$)	E_{pit} (V)
BM	0.02±0.10	0.22±0.14	-0.10±0.03	0.31±0.02	0.41±0.05
1.0% CO ₂	-0.10±0.03	0.17±0.06	-0.01±0.03	0.06±0.02	0.82±0.24
2.5% CO ₂	-0.10±0.10	0.71±0.07	-0.11±0.01	0.23±0.11	0.99±0.01

The corrosion rate (a function of i_{corr}) was found to be higher for the 2.5% CO₂ welding condition in comparison to the base material and 0% CO₂ welding condition. The actual value of 0.71 $\mu\text{A}/\text{cm}^2$ is low for the corrosion of stainless steels in acid media, compared *e.g.* with other welding processes [27], and indicates thus good corrosion resistance of the welds obtained in the present study. Concerning the uniform corrosion behavior in 3.5wt.% NaCl, different trends were observed relative to the 0.5M H₂SO₄ medium (Table 4). For the Cl⁻ containing electrolyte, the corrosion rates for the 2.5% CO₂ and AISI 316L base material were found to be in similar ranges, while for the 0% CO₂ weld lower corrosion rates were observed. These differences ought to be considered critically, however, since the active corrosion behavior of metal alloys is influenced by the various individual metal dissolution reactions such that the relatively small variations in i_{corr} which were observed are difficult to resolve.

The results obtained from the polarization diagrams in Figure 10(d) allow for a comparison in the pitting corrosion resistance, given the presence of Cl⁻ in the electrolyte. In this case, the welded samples were found to exhibit higher values of pitting corrosion resistance, with the pitting potential (E_{pit}) shifted to more positive values, in agreement with previous reports on the A-GTAW of stainless steels [28]. The pitting corrosion resistance of stainless steels has been linked with the presence of sulfide inclusions of a critical size ($\sim 1\mu\text{m}$) above which they act as pit initiation sites [27,29]. An analysis of the base material microstructure (Figure 11) reveals the presence of such typical inclusions can be identified. According to Stewart and Williams [29], the size and distribution of the sulfide particles are the principle factor controlling their role in pitting corrosion and not the actual sulfur content of the alloy. In the present study, the absence of large sulfide inclusions in the weld is probably caused by the fast cooling rate given the fact the relatively small size of the fusion zone relative to plate thickness (the welds did not reach full penetration).

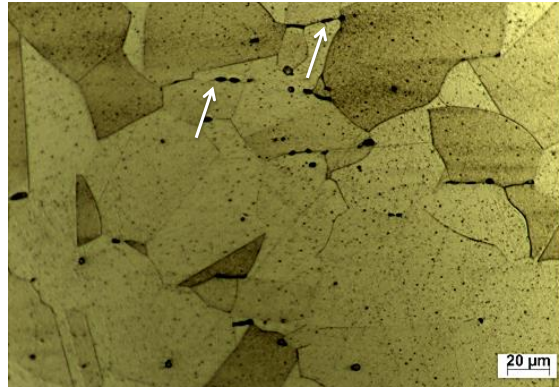


Figure 11. Microstructure of the AISI 316L base material showing the presence of inclusions (white arrows).

5. CONCLUSIONS

In the present work, a modified torch was developed for dual shielding composed of inert and active gases during GTAW. The proposed design allowed an increase in weld penetration, which can be attributed to the incorporation of oxygen in the weld pool during the process. Numerical analysis of the gas-flow in the modified torch indicated that the tungsten electrode would be protected by dual shielding, but this was confirmed only for relatively low active gas concentrations, which suggests the need for refining the simulation model employed. By employing a 2.5% CO₂ concentration on the outer gas layer, it was possible to obtain an increase in penetration-to-width ratio of approximately 3 times compared to the conventional GTAW setup with pure Ar shielding gas. The welds produced with 2.5% CO₂ dual shielding exhibited similar microstructure compared to conventional GTAW welds. The addition of CO₂ led to small increases in corrosion rate in acid media (from 0.22 ± 0.14 to 0.71 ± 0.07 $\mu\text{A}/\text{cm}^2$) and did not alter the behavior regarding uniform and pitting corrosion resistance in 3.5% NaCl aqueous solution.

ACKNOWLEDGEMENTS

This work was partially funded by the Coordenação de Aperfeiçoamento de Pessoal de Nível Superior - Brasil (CAPES) - Finance Code 001.

References

1. S. Lu, H. Fuji and K. Nogi, *Sci. Technol. Weld. Join.*, 14 (2009) 726.
2. M. Mirzaei, A. Khodabandeh and H. Najafi, *Trans. Indian Inst. Met.*, 69 (2016) 1723.
3. C.R. Heiple and J.R. Roper, *Weld. J.*, 61 (1982) 97.
4. C. Heiple and P. Burgardt, *Weld. Res. Suppl.*, 64 (1985) 159.
5. H. Fujii, T. Sato, S. Lu and K. Nogi, *Mater. Sci. Eng. A*, 495 (2008) 296.
6. S. Lu, H. Fujii, H. Sugiyama, M. Tanaka and K. Nogi, *Mater. Trans.*, 43 (2002) 2926.
7. G.H. Liu, M.H. Liu, Y.Y. Yi, Y.P. Zhang, Z.Y. Luo and L. Xu, *J. Cent. South Univ.*, 22 (2015) 800.

8. K.D. Ramkumar, P.S. Goutham, V.S. Radhakrishna, A. Tiwari and S. Anirudh, *J. Manuf. Process.*, 23 (2016) 231.
9. S. Leconte, P. Paillard and J. Saindrenan, *Sci. Technol. Weld. Join.*, 11 (2006) 43.
10. A. Berthier, P. Paillard and F. Christien, *Sci. Technol. Weld. Join.*, 14 (2009) 681.
11. R. Nakhaei, A. Khodabandeh and H. Najafi, *Acta. Metall. Sin. (English Lett.)*, 29 (2016) 295.
12. S. Lu, H. Fujii and K. Nogi, *Mater. Sci. Eng. A*, 380 (2004) 290.
13. S. Lu, H. Fujii and K. Nogi, *Metall. Mater. Trans. A Phys. Metall. Mater. Sci.*, 35 (2004) 2861.
14. X. Wang, J. Huang, Y. Huang, D. Fan and Y. Guo, *Appl. Therm. Eng.*, 113 (2017) 27.
15. S. Lu, H. Fujii and K. Nogi, *J. Mater. Sci. Technol.*, 26 (2010) 170.
16. Y. Zou, R. Ueji and H. Fujii, *Mater. Sci. Eng. A*, 620 (2014) 140.
17. Y. Morisada, H. Fujii and N. Xukun, *Mater. Des.*, 54 (2014) 526.
18. Y. Zou, R. Ueji and H. Fujii, *Mater. Charact.*, 91 (2014) 42.
19. S.W. Campbell, A.M. Galloway, G.M. Ramsey and N.A. McPherson, *J. Manuf. Sci. Eng.*, 135 (2013) 051016.
20. G.M. Ramsey, A.M. Galloway, S.W. Campbell, N.A. McPherson and T.J. Scanlon, *J. Mater. Process. Tech.*, 212 (2012) 1694.
21. E. Ahmadi and A.R. Ebrahimi, *J. Mater. Eng. Perform.*, 24 (2015) 1065.
22. C.X. Zhao, C. Kwakernaak, Y. Pan, I.M. Richardson, Z. Saldi, S. Kenjeres and C.R. Kleijn, *Acta Mater.*, 58 (2010) 6345.
23. X. Cai, C. Fan, S. Lin, X. Ji, C. Yang and W. Guo, *J. Mater. Process. Technol.*, 244 (2017) 225.
24. K.-H. Tseng and C.-Y. Hsu, *J. Mater. Process. Tech.*, 211 (2011) 503.
25. J.C. Lippold and D.J. Kotecki, *Welding Metallurgy and Weldability of Stainless Steels*, John Wiley & Sons, (2005) New Jersey, United States of America.
26. R. Mohammed, G. Madhusudhan Reddy, K. Srinivasa Rao, *Def. Tech.*, 11 (2015) 237.
27. R. Puli and G.D. Janaki Ram, *Corros. Sci.*, 62 (2012) 95.
28. M. Jurica, Z. Kožuh, I. Garašić and M. Bušić, *IOP Conf. Ser.: Materi. Sci. Eng.*, 329 (2018) 012012.
29. J. Stewart and D.E. Williams, *Corros. Sci.*, 33 (1992) 457.